

Visual and ultraviolet flux variability of the bright CP star θ Aurigae

J. Krtička¹, Z. Mikulášek¹, T. Lüftinger², and M. Japelka¹

¹ Department of Theoretical Physics and Astrophysics, Masaryk University, Kotlářská 2, 611 37 Brno, Czech Republic
e-mail: krticka@physics.muni.cz

² Institut für Astronomie, Universität Wien, Türkenschanzstraße 17, 1180 Wien, Austria

Received 2 October 2014 / Accepted 29 January 2015

ABSTRACT

Context. Chemically peculiar stars of the upper part of the main sequence show periodical variability in line intensities and continua, modulated by the stellar rotation, which is attributed to the existence of chemical spots on the surface of these stars. The flux variability is caused by the changing redistribution rate of the radiative flux predominantly from the short-wavelength part of the spectra to the long-wavelength part, which is a result of abundance anomalies. Many details of this process are still unknown.

Aims. We study the nature of the multi-spectral variability of one of the brightest chemically peculiar stars, θ Aur.

Methods. We predict the flux variability of θ Aur from the emerging intensities calculated for individual surface elements of the star taking into account horizontal variation of chemical composition. The surface chemical composition was derived from Doppler abundance maps.

Results. The simulated optical variability in the Strömgren photometric system and the ultraviolet flux variability agree well with observations. The IUE flux distribution is reproduced in great detail by our models in the near ultraviolet region. A minor disagreement remains between the observed and predicted fluxes in the far ultraviolet region. The resonance lines of magnesium and possibly also some lines of silicon are relatively weak in the ultraviolet domain, which indicates non-negligible vertical abundance gradients in the atmosphere. We also derive a new period of the star, $P = 3.618\,664(10)$ d, from all available photometric and magnetic measurements and show that the observed rotational period is constant over decades.

Conclusions. The ultraviolet and visual variability of θ Aur is mostly caused by silicon bound-free absorption and chromium and iron line absorption. Manganese also contributes to the variability, but to a lesser extent. These elements redistribute the flux mainly from the far-ultraviolet region to the near-ultraviolet and optical regions in the surface abundance spots. The light variability is modulated by the stellar rotation. The ultraviolet domain is key for understanding the properties of chemically peculiar stars. It provides a detailed test for surface abundance models and comprises many lines that originate from states with a low excitation potential, which enable detecting vertical abundance gradients.

Key words. stars: chemically peculiar – stars: early-type – stars: variables: general – stars: individual: θ Aurigae

1. Introduction

The atmospheres of main-sequence A and B stars are strongly affected by the radiative force. The radiative force acts selectively on some heavier elements, which leads to atomic diffusion and atomic segregation (Vauclair 2003; Michaud 2004). In normal AB stars the atomic diffusion is counteracted by the winds in hotter stars and by turbulence in cooler stars (Michaud et al. 2011), consequently, their abundance anomalies are only modest. The atmospheres of chemically peculiar (CP) stars are more stable, however, and consequently show distinct chemical composition remarkably different from the normal one (see Romanyuk 2007, for a review).

The magnetic field probably is the stabilizing force in a group of CP stars called magnetic chemically peculiar stars. In these stars the magnetic field of the order of hundreds of Gauss or higher dominates the whole atmosphere. Normal A stars may possibly also have a surface magnetic field, but with an intensity lower by two orders of magnitudes, as shown for Vega and Sirius (Lignières et al. 2009; Petit et al. 2011). Such weak fields do not significantly affect the atmospheres. There seems to be a clear dichotomy between stars with strong and weak magnetic fields (Aurière et al. 2007). Consequently, it seems that the so-called normal AB stars and the peculiar ones are in many respects very

similar apart from the strength of their anomalies (the strength of the magnetic field and the difference in chemical composition).

This view may be supported by the observation of the light variability of the A stars. The light variability of CP stars is caused by the flux redistribution due to bound-free (ionization, Peterson 1970; Lanz et al. 1996) and bound-bound (line, Wolff & Wolff 1971; Trasco 1972; Molnar 1973) transitions in surface abundance spots, which is modulated with stellar rotation. It is tempting to attribute the milli-magnitude variability observed in normal A stars (Balona 2013) to the same mechanism as in CP stars.

However, the test of this hypothesis is probably beyond the possibilities of current observational techniques. The situation in CP stars is much simpler. The theoretical light curves can be predicted using model atmospheres calculated with actual abundances from abundance maps of individual stars. A comparison of such theoretical light curves with observed ones supports the current picture of the light variability of CP stars (Krtička et al. 2009, 2012; Shulyak et al. 2010). This approach cannot be used for rotationally variable normal A stars because the expected abundance and line profile variations are prohibitively small for abundance mapping.

Consequently, studies of the light variability of AB stars should concentrate on CP stars with amplitudes of the order of

Table 1. IUE observations of θ Aur.

Image	SWP camera		Image	LWR camera	
	Julian date 2 400 000+	Phase		Julian date 2 400 000+	Phase
21 327	45 630.77975	0.068	2111	45 630.78658	0.070
21 331	45 631.04433	0.141	2135	45 632.79204	0.624
21 332	45 631.07042	0.148	2139	45 633.03122	0.690
21 353	45 632.79787	0.625	2150	45 634.82937	0.187
21 357	45 633.03467	0.691	2154	45 635.06043	0.251
21 358	45 633.06212	0.698	2166	45 636.79184	0.729
2 1375	45 634.79290	0.177	2184	45 638.78399	0.280
21 378	45 635.06294	0.251	2186	45 638.89943	0.312
21 390	45 636.78577	0.727			
21 412	45 638.77651	0.278			
21 414	45 638.90422	0.313			

Notes. Phases were calculated according to Eq. (6).

hundredths of magnitudes. But our knowledge is still far from complete even in this field. Most studies concentrate on hotter CP stars, ε UMa being the only example of a cooler CP star studied so far (Shulyak et al. 2010, based on maps of Lüftinger et al. 2003). Moreover, because we lack observational data in the UV, it is not always possible to couple the study of optical light variability with that of the UV spectral energy distribution variability. However, this is crucial for CP stars, in which the light variability originates in the UV, and the optical variations are just a glimpse of it.

To fill this gap, we here provide a study of the optical and UV flux variability of one of the brightest CP stars, θ Aur (HR 2095, HD 40312). This star belongs to a group of well-studied CP stars. The Balmer line spectroscopy revealed the influence of the Lorentz force on the stellar atmosphere of this star (Shulyak et al. 2007). The star is a frequent target of Doppler mapping (e.g., Khokhlova et al. 1986; Rice & Wehlau 1991; Kuschnig 1998b; Rice et al. 2004). We make use of the surface abundance maps of various elements derived using Doppler images by Kuschnig (1998a) and simulate the flux variability using model atmospheres.

2. Observations

θ Aur has been recognized as an A0p Si star by Cowley et al. (1969). The variability in UBV was established by Winzer (1974) and confirmed by two sets of $uvby$ measurements of Adelman (1997) and Adelman & Kaewkornmaung (2005). The star was also observed by HIPPARCOS in the Hp band (ESA 1997). The measurements of the effective magnetic field made by Landstreet & Borra (1977), Wade et al. (2000), and Silvester et al. (2012) represent further valuable phase information on the variability of θ Aur.

We supplemented these data by IUE spectra extracted from the INES database (Wamsteker et al. 2000, see Table 1) using the SPLAT package. We selected mostly high-dispersion large-aperture spectra in the domains 1150–1900 Å (SWP camera) and 2000–3000 Å (LWR camera). We used phase-dependent fluxes in our analysis. Moreover, we calculated artificial magnitudes from the spectra by convolving them with a Gaussian filter with a dispersion of 25 Å (for SWP spectra) and 100 Å (for LWR spectra).

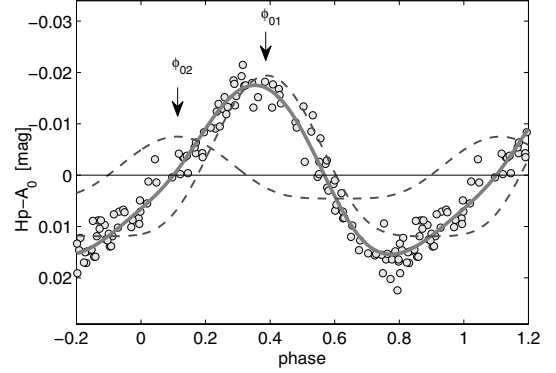


Fig. 1. Light curve of θ Aur in Hp fitted by the model light curve (full line), which is the sum of two partial light curves corresponding to individual spots (dashed lines) centred at φ_{01} and φ_{02} . Observations are denoted by circles.

3. Phenomenological modelling of the light and magnetic variability

The aim of the phenomenological modelling of the θ Aur light and magnetic field variability is to improve the rotational period of the star using all relevant sources of phase information, the few parametric descriptions of the light-curve shapes in the spectral domain from 1300 to 5500 Å, and to determine the magnetic field geometry.

3.1. Phenomenological model

We found that each of the studied 19 light curves with effective wavelengths from 1300 to 5500 Å is a smooth single wave curve, which can be approximated by a harmonic function of second order. Nevertheless, the shapes of the light curves in different bands are apparently different. We applied the weighted advanced principle component analysis (APCA) to the parameters of the harmonic fits, which allowed us to find hidden relationships among the individual light curves (for details see a brief introduction in Mikulášek 2007). We concluded that all light curves can well be expressed by a linear combination of only two principle components and that the amplitudes of the third and higher principal components are negligible.

This allowed us to build a relatively simple two-component phenomenological model with a minimum of free parameters valid for all studied light curves, where each of them is expressed by a linear combination of two principle normalized symmetrical functions (see Fig. 1). The models of the light curves are

$$F(\vartheta, \lambda) = A_{0k} - 2.5 \log_{10} I_{\lambda}, \quad (1)$$

where

$$I_{\lambda} = 1 + \sum_{j=1}^2 A_{j\lambda} \left\{ \exp \left[1 - \cosh \left(\frac{\varphi_j}{d_j} \right) \right] - 2.288 d_j \right\}. \quad (2)$$

The phase models are defined as

$$\vartheta = \frac{t - M_0}{P}; \quad \varphi_j = (\vartheta - \varphi_{0j}) - \text{round}(\vartheta - \varphi_{0j}), \quad j = 1, 2, \quad (3)$$

where ϑ is the so-called phase function (sum of the common phase φ and the epoch E , for details see Mikulášek et al. 2008) and t is the time in BJD. The origin of the phase function

Table 2. Phase data sources used in the phenomenological modelling of θ Aur variability.

Year		N	E_m	O–C	Source
1972	<i>UBV</i>	45	–2372	–0.07(7)	Winzer (1974)
1977	B_1	19	–1931	0.07(6)	Landstreet & Borra (1977)
1984	<i>IUE</i>	106	–1207	–0.05(10)	this paper
1992	<i>Hp</i>	131	–398	0.03(3)	ESA (1997)
1994	<i>wby</i>	188	–210	–0.02(2)	Adelman (1997)
1998	<i>C</i>	11	209	–0.07(4)	Wade et al. (2000)
2004	<i>wby</i>	276	859	–0.01(2)	Adelman et al. (2005)
2008	B_1	7	1206	0.00(2)	Silvester et al. (2012)

Notes. E_m is the mean epoch according to our ephemeris (see Eq. (6)). N is the number of observations.

(zero phase time) M_0 was fixed at 2 450 001.881 (the basic magnetic minimum according to Wade et al. 2000). P is the period (assumed to be constant), φ_{01} and φ_{02} are phases of centres of basic phase profiles (the phases of photocentres of photometric spots), d_1 and d_2 are the parameters expressing the width of the model spot profiles in phases, $A_{j\lambda}$ are the amplitudes of the light variations for the j th spot, φ_j is the phase counted from the centre of the j th profile, and A_{0k} is the mean magnitude of the k th set of observations from an individual author and an individual photometric colour.

The simplest phenomenological model of the phase curve of the longitudinal magnetic field (corresponding to the oblique central dipole) is the cosinusoid with the extrema at the phases when the magnetic poles are passing the stellar meridian. Nevertheless, the recent observations of the longitudinal magnetic field B_l of θ Aur indicate a more complex phase behaviour (see Wade et al. 2000; Silvester et al. 2012, and also Fig. 5). That is why we approximated the magnetic phase curve by the harmonic polynomial of the second order in the following special form, which allows us to estimate the extent of the distortion of the basic purely cosine course:

$$F(\vartheta) = \bar{B}_1 + A_3 \cos(2\pi\vartheta_3) + A_4 \cos(4\pi\vartheta_3) + A_5 \left[\sin(2\pi\vartheta_3) - \frac{1}{2} \sin(4\pi\vartheta_3) \right], \quad \vartheta_3 = \vartheta - \varphi_{03}, \quad (4)$$

where φ_{03} is the phase of the magnetic curve minimum, \bar{B}_1 is the mean longitudinal magnetic field, A_3 is the semi-amplitude of the cosine component of the magnetic variations. The semi-amplitudes A_4 and A_5 quantify the significance of the possible symmetrical/antisymmetrical distortions of the observed phase curve.

The model describes all observed light curves obtained in 18 different photometric colours and magnetic variations with a fairly high fidelity with only 67 free parameters. This phenomenological model was applied to observational data representing 771 individual measurements. The measurements more or less evenly cover the time interval 1971–2008 (see Table 2), and consist of three sets of magnetic measurements, *UBV* observations, two sets of *wby* measurements, *Hp* photometry, and 106 mag in 11 ultraviolet wavelengths derived from *IUE* spectra (see Sect. 2).

We determined individual parameters \mathbf{a} and their uncertainties of the model described by Eqs. (1) and (4) by deriving for each measurement its model prediction $F(t_i, \mathbf{a})$ using the standard weighted least-square method applied to the set of

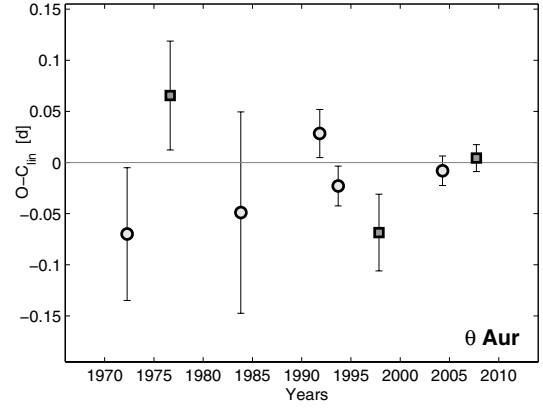


Fig. 2. O–C diagram of θ Aur indicates that its period is nearly constant. Circles indicate O–Cs derived from photometry, squares correspond to O–Cs found from magnetic measurements.

measured values (magnitude, magnetic field) y_i , with the estimated uncertainty σ_i ,

$$\Delta y_i = y_i - F(t_i, \mathbf{a}); \quad \chi^2 = \sum_{i=1}^n \left(\frac{\Delta y_i}{\sigma_i} \right)^2; \\ \nabla \chi^2 = \mathbf{0}; \quad \Rightarrow \quad \sum_{i=1}^n \frac{\Delta y_i}{\sigma_i^2} \nabla_{\mathbf{a}} F(t_i, \mathbf{a}) = \mathbf{0}. \quad (5)$$

For details see also Mikulášek et al. (2011a).

3.2. New ephemeris and O–C diagram

One of the principle results of our phenomenological modelling was the improved period of the observed stellar variations: $P = 3^d 618\,664(10)$. The time of the zero phase and the zero epoch, $M_0 = 2\,450\,001.881$, were adopted from the ephemeris published in Wade et al. (2000). The times of the zero phase $\Theta(E)$ can be approximated by the relation

$$\Theta(E) = 2\,450\,001.881 + 3^d 618\,664(10) \times E, \quad (6)$$

where E is the integer, also called the epoch. The period agrees well with other determinations (Wade et al. 2000; Adelman & Kaewkornmaung 2005). The phase shift between this ephemeris and that used by Kuschnig (1998a) in the time of their spectral observations is $\Delta\varphi = -0.268$.

We also tested a possible period variability. We assumed that the phase function is approximated by the relation

$$\vartheta = \frac{t - M_0}{P_0} - \frac{\dot{P}}{2} \left(\frac{t - M_0}{P_0} \right)^2; \quad \Theta = M_0 + P_0 E + \frac{\dot{P} P_0 E^2}{2}, \quad (7)$$

where P_0 is the instant period at M_0 and \dot{P} is the time derivative of the period. We found that $\dot{P} = 3(5) \times 10^{-9}$, so we can conclude that there is zero quadratic term in the θ Aur ephemeris and the period is constant.

A more complex behaviour of the period can be revealed by means of the O–C diagram inspection. The phase function can be approximated by the relation

$$\vartheta(t, r) = \frac{t - M_0 - (\text{O–C})_r}{P_0}, \quad (8)$$

where M_0 and P_0 are fixed, $P_0 = 3^d 618\,664$, and $(\text{O–C})_r$ are the mean O–C values of the subsets r of the observational data (for details see in Mikulášek et al. 2011b). The O–C diagram in Fig. 2 (constructed using observations in Table 2) does not indicate any period variations during the past 33 yr.

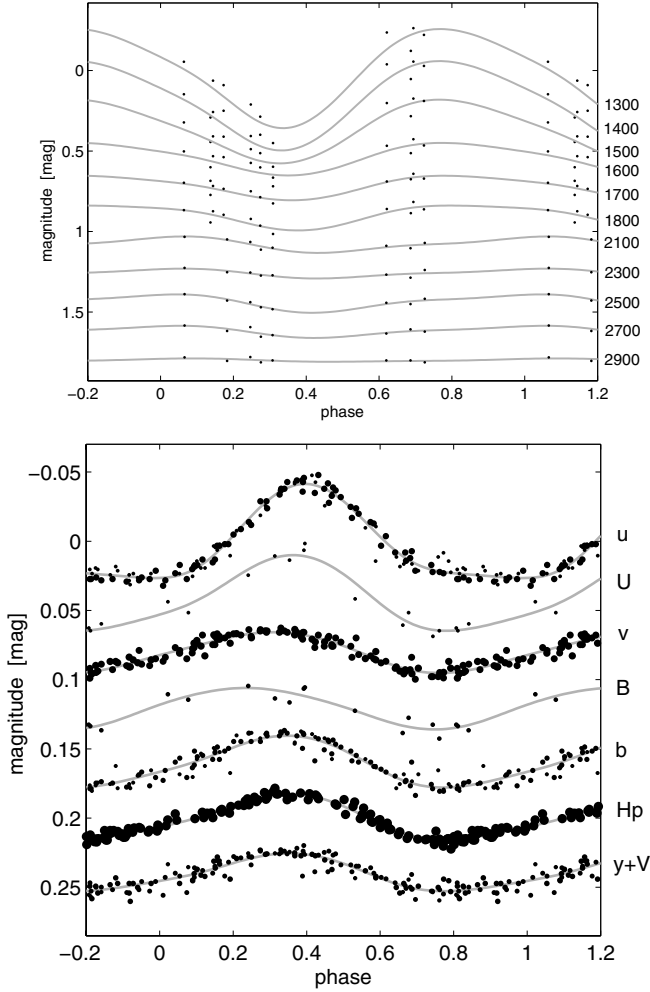


Fig. 3. Observed light curves of θ Aur in UV (*upper panel*) and in standard photometry (*lower panel*). Symbols on the right side denote the effective wavelengths in \AA or a filter. Point areas in the lower panel correspond to the weight of measurements. Grey lines are the results of phenomenological modelling.

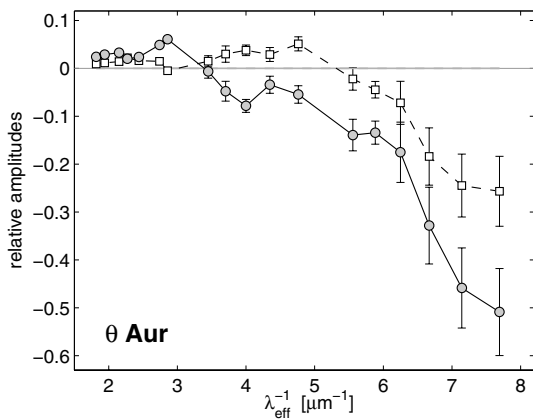


Fig. 4. Amplitudes of two photometric spots centred at $\varphi_{02} = 0.11$ (squares) and $\varphi_{01} = 0.39$ (full dots) at various wavelengths.

3.3. Light curves

We present the light curves of θ Aur in the region 1300–5500 \AA , which covers a substantial part of the stellar flux, in Fig. 3. The largest amplitudes are shown by the light curves at the short-wavelength end of the spectral region. The phenomenological

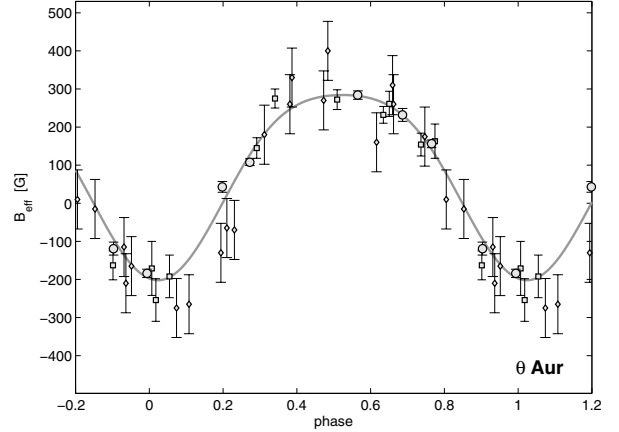


Fig. 5. Variations of the longitudinal component of the magnetic field of θ Aur. Squares denote the observation of Wade et al. (2000), diamonds the observation of Landstreet & Borra (1977), and circles the observation of Silvester et al. (2012). The grey line is the symmetric model fit.

modelling of the light curve set by the linear combination of two basic symmetric phase profiles (see Eq. (1)) was successful, the model is able to plausibly fit the shapes of all observed light curves. The dominant feature of the spectrum is centred at the phase $\varphi_{01} = 0.389(4)$. Our test showed that the width d_2 of the second profile centred at $\varphi_{02} = 0.112(10)$ is nearly identical to the width of the first profile. Consequently, we assumed that the widths of all phase structures are the same, $d_1 = d_2 = d = 0.165(3)$.

The observed behaviour of light curves can be interpreted by the presence of two dominant photometric spots on the surface of the rotating star whose photo-centres pass the stellar median at phases 0.389 and 0.110. The contrasts of the spots with respect to their surroundings and the contrast of the spots themselves determine the shape of the light curve in a particular photometric colour. The principle spot is bright only for wavelengths longer than 3400 \AA , otherwise it is dark. The second spot is bright for wavelengths longer than 1850 \AA . For shorter wavelengths, both spots are dark, and together they create one extensive shady feature.

3.4. Geometry of the magnetic field and its relation to photometric spots

The magnetic field variations are described by the model Eq. (4). The phase of the sharp magnetic minimum is $\varphi_{03} = 0.024(4)$. The mean value of the longitudinal component of the magnetic induction of θ Aur is positive ($\bar{B}_1 = 85(4)$ G), which means that the positive pole of the magnetic dipole is in the northern hemisphere of the star. The derived semi-amplitude of magnetic variations is $A_3 = -243(7)$ G, and the semi-amplitude of the symmetrical component $A_4 = -44(5)$ G is nonzero, contrary to the semi-amplitude of the antisymmetric term $A_5 = -8(10)$ G. This means that the phase curve of the magnetic variations is definitely distorted, but symmetric around the phase of the magnetic minimum (see Fig. 5). This form of the phase curve can be explained by assuming that the magnetic dipole is slightly shifted from the centre in the direction of the negative magnetic pole.

The phases of the centres of assumed photometric spots neither coincide with the phases of magnetic field extrema nor with phases when the magnetic equator passes the centre of the visible

Table 3. θ Aur parameters derived by Kuschnig (1998a).

Effective temperature T_{eff}	10 500 K
Surface gravity $\log g$ (cgs)	3.5
Inclination i	60°
Rotational velocity projection $v_{\text{rot}} \sin i$	55 km s ⁻¹
Stellar radius ¹ R_*	4.34(5) R_{\odot}
Helium abundance	-2.8 < ϵ_{He} < -1.9
Magnesium abundance	-7.5 < ϵ_{Mg} < -3.2
Silicon abundance	-3.6 < ϵ_{Si} < -2.8
Titanium abundance	-7.9 < ϵ_{Ti} < -6.9
Chromium abundance	-6.0 < ϵ_{Cr} < -3.4
Manganese abundance	-6.2 < ϵ_{Mn} < -4.7
Iron abundance	-4.2 < ϵ_{Fe} < -3.2
Strontium abundance	-9.1 < ϵ_{Sr} < -7.7

Notes. ⁽¹⁾ Derived in Sect. 7.

stellar disc. Moreover, the spots with the highest element abundances mapped by Kuschnig (1998a) appear on the visible disc around the phases 0.3–0.4, again showing a mismatch with the surface magnetic field. Thus we conclude that there is no obvious connection between the photometric structures on the stellar surface and the stellar magnetic field geometry.

4. Calculating the flux variability

4.1. Model atmospheres and synthetic spectra

The stellar parameters of θ Aur together with the range of surface abundances of individual elements taken from Kuschnig (1998a) are given in Table 3. The effective temperature and surface gravity were derived from fitting the H δ lines. The projected rotational velocity was derived from spectroscopy. The range of surface abundances was extracted from surface abundance maps, which were derived by Doppler imaging. In our study the abundances are defined relative to hydrogen, that is, $\epsilon_{\text{el}} = \log(N_{\text{el}}/N_{\text{H}})$.

We used the code ATLAS12 for the model atmosphere calculations (Kurucz 2005; Castelli 2005). For each model atmosphere we calculated the synthetic spectrum using the code SYNSPEC with atomic data from Lanz & Hubeny (2007). The adopted SYNSPEC line list was enlarged by the data for chromium and iron taken from Kurucz (2009)¹. We computed angle-dependent emerging intensities for 20 equidistantly spaced values of $\mu = \cos \theta$, where θ is the angle between the normal to the surface and the line of sight.

In our models we assumed fixed effective temperature and surface gravity (see Table 3) and adopted a generic value of the microturbulent velocity $v_{\text{turb}} = 2$ km s⁻¹. The abundance of Mg, Si, Cr, Mn, and Fe was selected according to the surface abundance maps (see below). We assumed solar abundance of the other elements (Asplund et al. 2009).

The model atmospheres and the angle-dependent intensities $I(\lambda, \theta, \epsilon_{\text{Mg}}, \epsilon_{\text{Si}}, \epsilon_{\text{Cr}}, \epsilon_{\text{Mn}}, \epsilon_{\text{Fe}})$ were calculated for a five-parametric grid of magnesium, silicon, chromium, manganese, and iron abundances (given in Table 4). For silicon and iron this grid fully covers the range of abundances found on the surface of θ Aur (Table 3). For magnesium, chromium, and manganese the lowest abundances were omitted from the grid because these elements with such low abundance do not influence the emerging fluxes. This helped us to significantly reduce the

Table 4. Individual abundances ϵ_{Mg} , ϵ_{Si} , ϵ_{Cr} , ϵ_{Mn} , and ϵ_{Fe} of the model grid.

Mg	-4.1	-3.6	-3.1			
Si	-3.7	-3.2	-2.7			
Cr	-5.9	-5.4	-4.9	-4.4	-3.9	-3.4
Mn	-5.7	-5.2	-4.7			
Fe	-4.2	-3.7	-3.2			

Table 5. Coefficients of analytical fits of the photonic passbands of the Strömgren photometric system filters *uvby* Eqs. (11) and (12).

	a_1	a_2	a_3	a_4	a_5	a_6	d_c	σ_c
u	21.3	-14.3	3590	8.85	448	-1430	3475	10 ³
v	94.4	-652	2000	55.2	305	0	4100	10 ³
b	76.7	-268	0	111	-896	2790	4675	10 ³
y	24.8	465	0	47.1	578	0	5475	10 ³

required computer time. Our test showed that the highest abundances of helium, titanium, and strontium on the surface of θ Aur (see Table 3) are so low that they do not influence the emerging flux. Consequently, these elements were excluded from the grid of calculated abundances in Table 4, and we only assumed a surface mean abundance of these elements.

4.2. Phase-dependent flux distribution

The derived grid of spectra (Table 4) was used to calculate the radiative flux in a bandpass c at the distance D from the star (Mihalas 1978)

$$f_c = \left(\frac{R_*}{D}\right)^2 \int_{\text{visible surface}} I_c(\theta, \Omega) \cos \theta \, d\Omega. \quad (9)$$

The intensity $I_c(\theta, \Omega)$ at angle θ with respect to the normal at the surface was obtained at each surface point with spherical coordinates Ω by interpolating between the intensities $I_c(\theta, \epsilon_{\text{Mg}}, \epsilon_{\text{Si}}, \epsilon_{\text{Cr}}, \epsilon_{\text{Mn}}, \epsilon_{\text{Fe}})$ calculated from the grid as

$$I_c(\theta, \epsilon_{\text{Mg}}, \epsilon_{\text{Si}}, \epsilon_{\text{Cr}}, \epsilon_{\text{Mn}}, \epsilon_{\text{Fe}}) = \int_0^{\infty} \Phi_c(\lambda) I(\lambda, \theta, \epsilon_{\text{Mg}}, \epsilon_{\text{Si}}, \epsilon_{\text{Cr}}, \epsilon_{\text{Mn}}, \epsilon_{\text{Fe}}) \, d\lambda. \quad (10)$$

The response function $\Phi_c(\lambda)$ of a given bandpass c is a Gauss function for the UV magnitudes (the same as for IUE fluxes, see Sect. 2). For the Strömgren photometric system we use analytical fits to photonic passbands from Bessell (2011),

$$\Phi_c(\lambda) = \begin{cases} \exp\{-x[a_{1c} + x(a_{2c} + a_{3c}x)]\}, & x < d_c, \\ \exp\{-x[a_{4c} + x(a_{5c} + a_{6c}x)]\}, & x > d_c, \end{cases} \quad (11)$$

where

$$x = \frac{(\lambda - d_c)^2}{\sigma_c^2}, \quad (12)$$

where λ is the wavelength in Å. The coefficients of the fits are given in Table 5.

The magnitude difference between the flux f_c at a given phase and the reference flux f_c^{ref} in bandpass c is defined as

$$\Delta m_c = -2.5 \log \left(\frac{f_c}{f_c^{\text{ref}}} \right). \quad (13)$$

The reference flux is obtained under the condition that the mean magnitude difference over the rotational period is zero.

¹ <http://kurucz.harvard.edu>

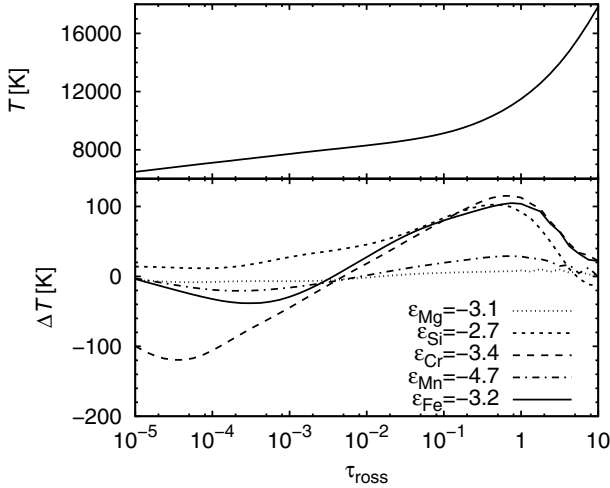


Fig. 6. *Upper plot:* temperature dependence on the Rosseland optical depth τ_{ross} in the reference model atmosphere with $\epsilon_{\text{Mg}} = -4.1$, $\epsilon_{\text{Si}} = -3.7$, $\epsilon_{\text{Cr}} = -4.4$, $\epsilon_{\text{Mn}} = -5.7$, and $\epsilon_{\text{Fe}} = -4.2$. *Lower plot:* difference between temperature in the model atmospheres with abundance of the selected element enhanced by a factor of 10 and the temperature in the reference model atmosphere.

5. Influence of heavier elements on atmospheric structure

Heavier elements significantly affect the structure of stellar atmospheres. Although their abundance is much smaller than that of hydrogen even in CP stars, their contribution to opacity is crucial. Bound-free transition of silicon and numerous line transitions of iron group elements (in our case, chromium and iron) are able to absorb the stellar radiation, which leads to heating of continuum-forming regions ($\tau_{\text{ross}} \approx 0.1$ – 1). This is shown in Fig. 6, where we plot the temperature difference between the models with enhanced abundance of a selected element by a factor of 10 and a reference one.

The heavier elements also lead to a redistribution of the emerging flux typically from the far UV to the near UV region and to the optical domain. This is shown in Fig. 7, where we compare the emerging fluxes calculated in a model with enhanced abundance of the selected element by a factor of 10 and the reference one. Silicon redistributes the far UV flux to the spectral regions with $\lambda > 1700$ Å. The influence of chromium and iron on the emerging flux is more complex, but in general, these elements redistribute the flux from the far UV region to the spectral region with $\lambda \gtrsim 2900$ Å. Magnesium and manganese do not affect the emergent flux significantly.

The flux changes caused by the heavier elements manifest themselves in the changes of the apparent magnitude. This can be seen from the plot of the magnitude difference

$$\Delta m_{\lambda} = -2.5 \log \left(\frac{H_{\lambda}(\epsilon_{\text{Mg}}, \epsilon_{\text{Si}}, \epsilon_{\text{Cr}}, \epsilon_{\text{Mn}}, \epsilon_{\text{Fe}})}{H_{\lambda}^{\text{ref}}} \right), \quad (14)$$

in Fig. 8. H_{λ}^{ref} is the reference flux calculated for $\epsilon_{\text{Mg}} = -4.1$, $\epsilon_{\text{Si}} = -3.7$, $\epsilon_{\text{Cr}} = -4.4$, $\epsilon_{\text{Mn}} = -5.7$, and $\epsilon_{\text{Fe}} = -4.2$. For silicon the magnitude difference decreases with increasing wavelength. There is a minimum of Δm_{λ} at about 5200 Å for iron and at 5400–5600 Å for chromium, supporting the conclusion that these elements significantly contribute to the flux depression at these wavelengths (Kupka et al. 2003; Khan & Shulyak 2007; Krtićka et al. 2009). As follows already from Fig. 7, magnesium

and manganese do not significantly affect the emerging fluxes in the case studied here.

6. Predicted broad-band variations

Different parts of the stellar surface are exposed to the observer as a result of the stellar rotation, which causes the stellar light variability. To account for the stellar rotation, predicted light curves were calculated from Eq. (13) as a function of the rotational phase.

In Fig. 9 we provide the light variations calculated from the abundance map of one element alone assuming a fixed abundance of other elements ($\epsilon_{\text{Mg}} = -4.1$, $\epsilon_{\text{Si}} = -3.7$, $\epsilon_{\text{Cr}} = -5.9$, $\epsilon_{\text{Mn}} = -5.7$, and $\epsilon_{\text{Fe}} = -4.2$). From Fig. 9 it follows that mainly silicon, chromium, iron, and partly manganese cause the light variability. These elements are able to affect the emerging flux, and there is a large overabundance of these elements in the spots. The light curves of individual elements reflect the variations of line equivalent widths. As a result of the different surface distribution of individual elements, the line equivalent widths curves and also individual light curves in Fig. 9 differ in shape.

Silicon bound-free absorption dominates the flux distribution below roughly 1700 Å. The absorbed flux is redistributed to longer wavelengths, consequently, the silicon flux variations at 1300 Å and 2500 Å are in anti-phase in Fig. 9. For similar reasons, the UV flux variations and the visual light variations are in anti-phase for chromium, manganese, and iron.

Taking into account the surface distribution of all significant elements (see Table 4), the observed and predicted light curves in the b and y filters of the Strömgren photometric system agree well in Fig. 10. The observed curves have slightly lower amplitudes than the predicted curves in the v filter, whereas there is also a slight phase shift between these curves in the u filter. A similar behaviour also appears in the UV light curves in Fig. 11. Here we plot the observed and predicted light curves, which were processed using a Gaussian filter. The observed and predicted light curves agree very well in the long-wavelength part of the UV spectrum with $\lambda \geq 1600$ Å, whereas the observed curves have lower amplitudes than the predicted curves in the far-UV domain with $\lambda \leq 1500$ Å.

The inhomogeneous surface distribution of individual elements causes bright spots on the stellar surface. The spots, whose surface distribution can be derived using abundance maps and model atmospheres (see Fig. 12), cause the light variability. Given the relative proximity of the star, θ Aur can be an ideal candidate for interferometric analysis (cf. Shulyak et al. 2014).

7. Ultraviolet flux variations

We have shown that most of the light variability of θ Aur can be explained by the flux redistribution from far UV to the near UV and visible regions. This is supported by the comparison of UV and visual light curves, which are typically in anti-phase. However, there is some disagreement between observed and predicted light curves. The predicted u -amplitude is too low (Fig. 10) and, in addition, the predicted variations in the far-UV are stronger than the observed variations (Fig. 11). Further discussion of ultraviolet fluxes is necessary to understand the origin of these differences.

In Fig. 13 we compare the observed and the predicted fluxes smoothed by a Gaussian filter with a dispersion of 10 Å. We normalized the predicted fluxes by a multiplicative factor, which

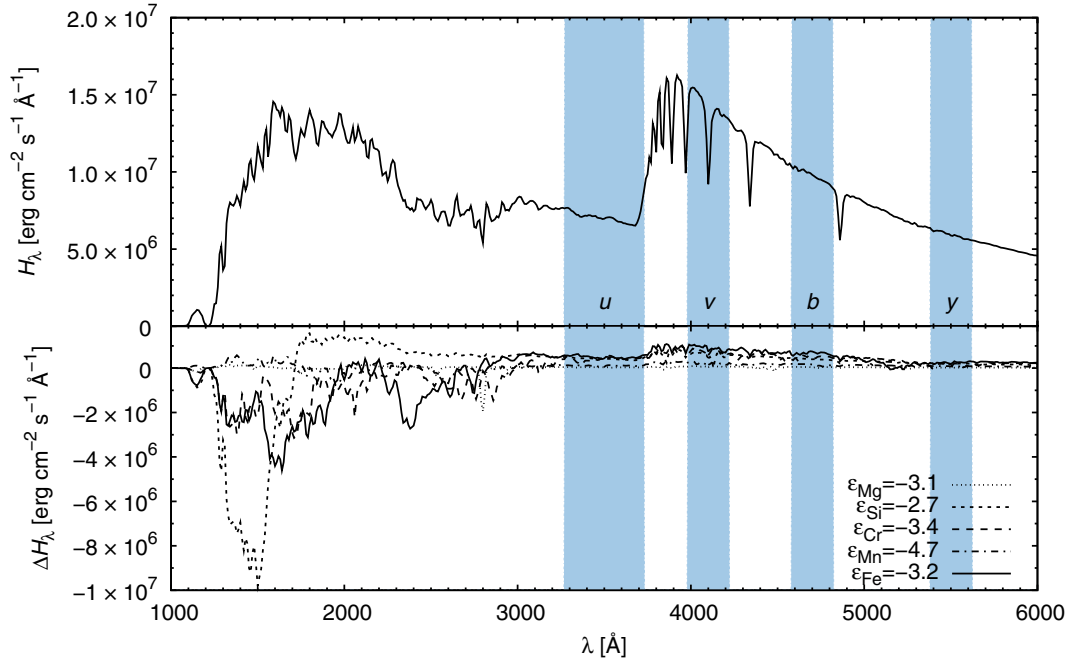


Fig. 7. Upper plot: emerging flux from a reference model atmosphere ($\epsilon_{\text{Mg}} = -4.1$, $\epsilon_{\text{Si}} = -3.7$, $\epsilon_{\text{Cr}} = -4.4$, $\epsilon_{\text{Mn}} = -5.7$, and $\epsilon_{\text{Fe}} = -4.2$). Lower plot: difference between the emerging flux from the model atmospheres with higher abundance of the selected element by a factor of 10 and the flux from a reference model. All fluxes were smoothed by a Gaussian filter with a dispersion of 10 \AA to show the changes in continuum. The passbands of the *uwby* photometric system are also denoted.

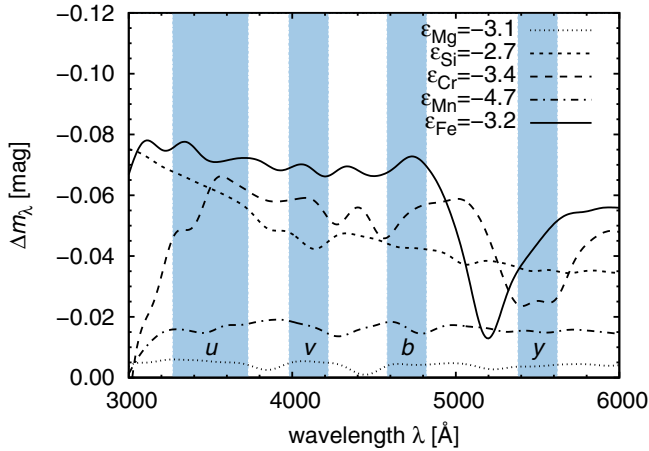


Fig. 8. Magnitude difference Δm_λ between the emerging fluxes calculated with an enhanced abundance (by a factor of 10) of a selected element and the reference flux H_λ^{ref} (Eq. (14)). The fluxes were smoothed by a Gaussian filter with a dispersion of 100 \AA .

yields the best match between observations and predictions in Fig. 13. The factor was kept fixed for all wavelengths in all subsequent calculations.

From the UV flux normalization we derived the stellar radius $R = 4.34 \pm 0.05 R_\odot$ assuming a distance of $50.8 \pm 0.4 \text{ pc}$ (van Leeuwen 2007). This is significantly higher than the $2.2 R_\odot$ reported by Pasinetti Fracassini et al. (2001) or the $3.3 R_\odot$ derived by Babu (1977). On the other hand, our value agrees with the radius of $4.3 R_\odot$ adopted by Rice et al. (2004). Moreover, our derived radius yields with the rotational period and inclination given in Table 3 the projection of the rotational velocity $v_{\text{rot}} \sin i = 53 \text{ km s}^{-1}$, which agrees with observations (see Table 3).

The mean predicted and observed fluxes agree very well in the near-UV region with $\lambda > 2000 \text{ \AA}$ (see Fig. 13). However, the mean predicted flux is slightly lower than the observed one in the region $1250\text{--}1500 \text{ \AA}$. The opposite is true in the region between $1700\text{--}1900 \text{ \AA}$. On the other hand, the amplitude of the flux variations agrees well with observations in the whole UV domain except for the region of $2000\text{--}2300 \text{ \AA}$.

This is further shown in Fig. 14, where we compare predicted and observed fluxes for selected phases. The fluxes agree very well in the near-UV region with $\lambda > 1900 \text{ \AA}$. The shape of the pseudo-continuum (formed by thousands of metallic lines) and the strongest line blends of mostly chromium and iron agree very well. The only exception is the Mg II doublet at 2800 \AA , whose line depth is overestimated by the spectrum synthesis.

The fluxes in the far-UV region agree less well. The predicted flux is underestimated in the far UV region with $\lambda < 1500 \text{ \AA}$ with an exception of the phase around $\varphi = 0.7$. Moreover, the observations show a stronger line absorption in the region $1700\text{--}1800 \text{ \AA}$, which is not explained by the models.

The fact that the observed and predicted fluxes most strongly disagree in the region with $\lambda < 1500 \text{ \AA}$, where the silicon strongly influences the flux distribution (see Fig. 7) points to a possible problem with the silicon abundance map. This might be connected with the relatively few spectra that were used to derive the maps (13). This might also explain the shift between predicted and observed UV light curves in the bands with $\lambda \leq 1500 \text{ \AA}$ (see Fig. 11). On the other hand, the stronger line absorption in the region $1700\text{--}1800 \text{ \AA}$ is connected with missing line opacity in the models, either caused by some element that was excluded from the mapping or by an incompleteness of the current line lists.

A too strong predicted Mg II doublet at 2800 \AA can be caused by a vertical abundance distribution of magnesium. This is a

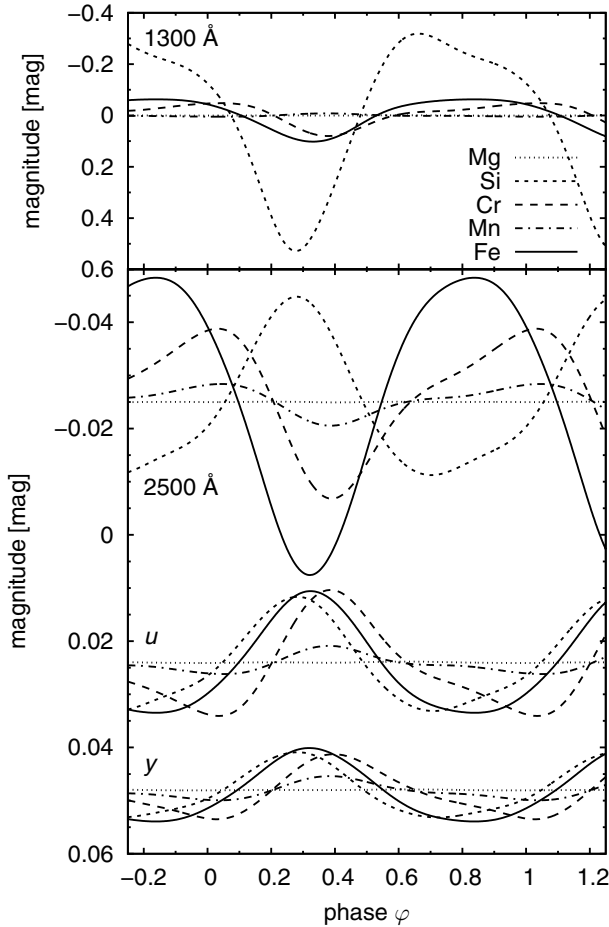


Fig. 9. Predicted UV and visual flux variations of θ Aur calculated using abundance maps of one element alone. The abundance of other elements was fixed. Light curves for selected wavelengths in the UV domain (denoted in the graph) were calculated using a Gaussian filter with a dispersion of 100 Å. The light variations were calculated for the u and y filters of the Strömgren photometric system. Light curves in individual bands were vertically shifted to better show the variability.

resonance doublet, whereas the 4481 Å line used by [Kuschnig \(1998a\)](#) for surface abundance mapping originates from excited levels, where the lower-level energy of the corresponding transition is 8.9 eV. A similar effect, but weaker, is also visible in some Si II lines. Vertical abundance gradients are frequently found in other CP stars (e.g., [Lüftinger et al. 2008](#); [Ryabchikova et al. 2008](#); [Nesvacil et al. 2013](#); [Bailey & Landstreet 2013](#)). Moreover, the carbon line blend at 1335 Å shows an equivalent width variability, which suggests an inhomogeneous surface distribution of this element.

From Fig. 13 it follows that even the mean observed UV flux does not correspond to the solar chemical composition. Especially the observed far-UV flux is significantly lower than the solar flux. This flux decline can presumably not be modelled without reliably knowing the surface abundance distribution. This makes the temperature determination of CP stars from the UV spectra problematic.

8. Detailed comparison of observed and predicted light curves

We conclude that the predicted light curves explain the nature of the photometric variability of θ Aur, but the correspondence

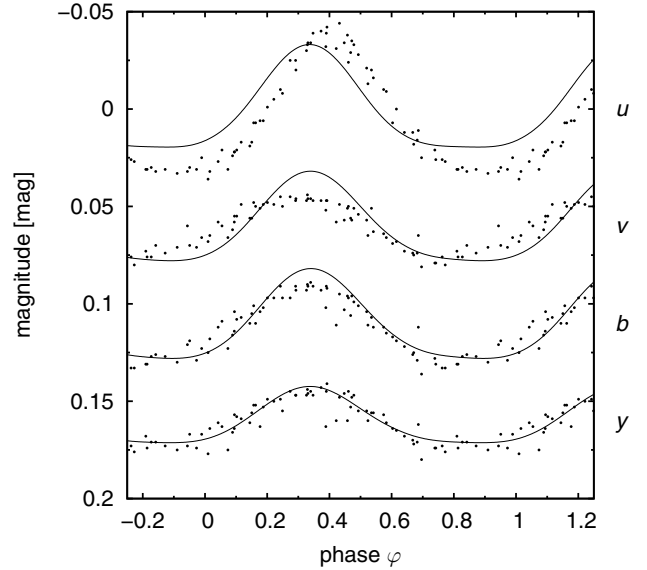


Fig. 10. Predicted light variations of θ Aur (solid lines) in the Strömgren photometric system computed taking the surface distribution of all elements. The observed light variations (dots) are taken from [Adelman & Kaewkornmaung \(2005\)](#). The light curves in individual filters were vertically shifted to better show the light variability.

is not excellent. The physical model, for example, does not agree with all results obtained by the phenomenological model described and discussed in Sect. 3, especially the incidence and properties of the second photometric spot centred at the phase 0.11.

Although we see a large scatter in the ratio of the observed and predicted amplitudes of light variations (see Fig. 15), the real light variability of the star is weaker than predicted. This might be because some important sources of photometric variability were neglected, because including additional variability sources results in a less important role of the remaining sources. The other possibility is that the variability caused by silicon is too large. Nevertheless, there are some interesting exceptions – the relatively strong enhancement of the observed amplitude in the photometric band u , where some mechanisms connected with the nearby Balmer jump might be important.

The phase shift between the observed and predicted light curves in Fig. 16 provides additional information about the agreement between observed and predicted light curves. The shift in the optical region decreases with increasing frequency, and in the region of the Balmer jump, it suddenly switches to a large positive shift. The phenomenological model explains this phenomenon by strong changes in the amplitude of the secondary spot, which reaches its highest brightness before the Balmer jump and almost vanishes after the jump. Trends in the shift in other parts of the figure can be also explained by the wavelength dependency of the contrast of the secondary spot.

The predicted light curves are based on the horizontal elemental abundance variations derived from observations. However, CP stars also show vertical abundance gradients, which in θ Aur are probably evidenced in some UV line profiles. It is possible that the emerging flux at different wavelengths originates in different vertical regions. Consequently, the vertical abundance gradients in the atmosphere may in principle affect the light curves, and neglecting vertical abundance gradients may be one of the reasons for the disagreement between theoretical and observed light curves.

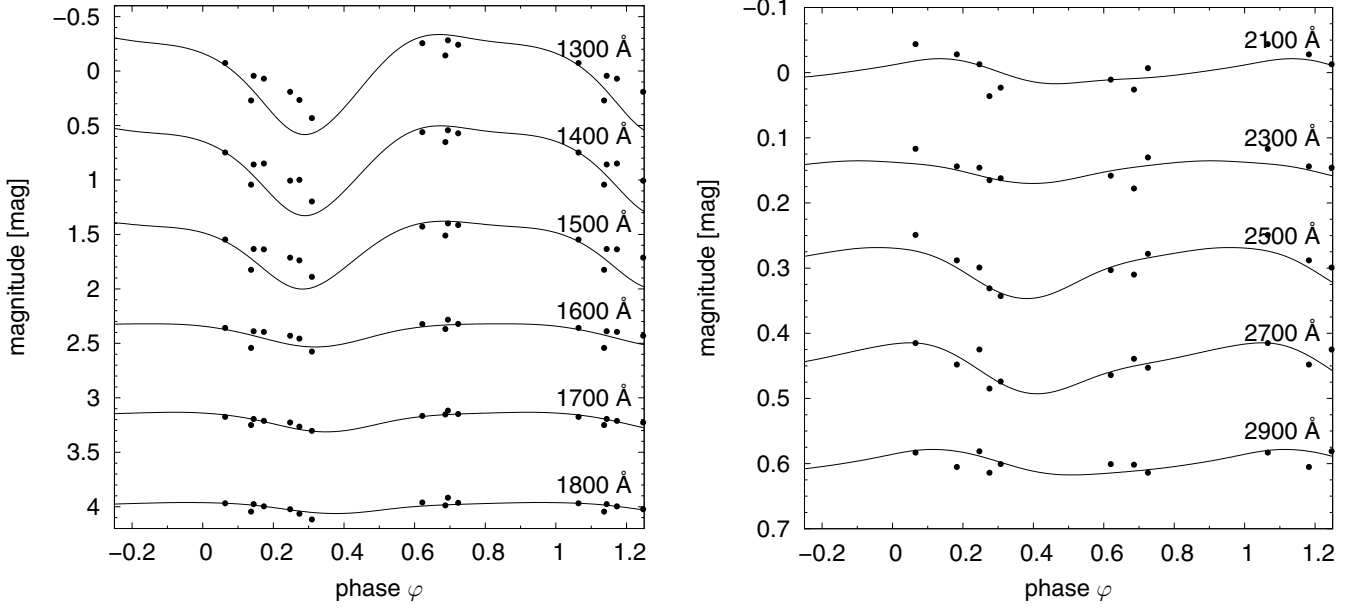


Fig. 11. Comparison of the predicted (solid line) and observed (dots) UV light variations for different wavelengths (marked in the graph). The light curves were derived from IUE spectra using a Gaussian filter with a dispersion of 25 Å (for SWP spectra) and 100 Å (LWR spectra). Curves for individual wavelengths were vertically shifted to better show the variability.

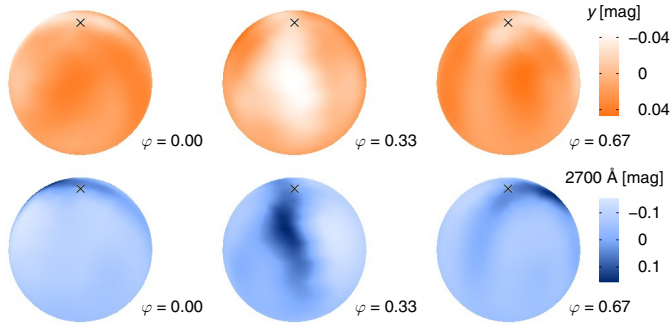


Fig. 12. Emerging intensity from individual surface elements of θ Aur at various rotational phases. *Upper panel:* visible y band. *Lower panel:* UV band centred at 2700 Å. Both for $\mu = 1$.

9. Conclusions

We successfully simulated the UV and visual flux variability of the chemically peculiar star θ Aur. We assumed that the variability is caused by the inhomogeneous surface distribution of chemical elements. We used model atmospheres calculated with appropriate abundances corresponding to the Doppler maps of Kuschnig (1998a) to predict the light variability.

We also used our phenomenological model to improve the rotational period of the star and to model the light curves in the spectral region 1300–5500 Å. The phenomenological model assumes two photometric spots with distinct optical characteristics. We determined the geometry of the magnetic field and showed that there is no obvious connection between the field and photometric spots on the stellar surface.

The numerical simulations based on the Doppler maps and model atmospheres explain most of the variability of θ Aur. Heavier elements influence the emerging flux through flux redistribution mainly from the far-UV to near-UV and visible regions. The bound-free transitions of silicon and the bound-bound transitions of chromium, iron, and to a lesser extent manganese mostly cause the flux redistribution and variability in θ Aur. As

a result of the flux redistribution and inhomogeneous elemental surface distribution, the individual surface elements display different brightnesses in individual spectral regions. The total observed flux, which is given by integrating over the whole stellar surface, is modulated by the stellar rotation. Resulting simulated light curves were compared with synthetic colours derived from IUE spectroscopy and with observed variability in bands of the Strömgren photometric system.

The inhomogeneous surface distribution of silicon, chromium, manganese, and iron is able to explain most of the observed UV and visible flux variations. We reproduced the anti-phase behaviour of the light curves in the far-UV and visible regions. The light curve amplitude is about a few hundredths of a magnitude in the visual domain, while it reaches nearly 1 mag in the UV. There remains some minor disagreement between the predicted and observed light curves, particularly in the u colour of the Strömgren photometric system or in the far-UV band at 1300 Å.

Our models reproduce the observed spectral energy distribution in the near-UV region in detail. The absorption features that resemble strong lines in this region are in fact mostly blends of numerous iron and chromium lines. The spectral energy distribution in the far-UV region is only well reproduced around the phase of $\varphi = 0.7$. There are minor differences in other phases, which may be connected with a coarser phase coverage of the spectra used to prepare the silicon abundance maps. Other discrepancies in the far-UV may be attributed to some missing line opacity in the models.

The UV spectral analysis is very well suited for detecting vertical abundance gradients. The UV region comprises many strong lines that originate from states with low excitation potential, which provides information about the upper parts of the atmosphere. In combination with an optical analysis (on which the Doppler maps are based), which also yields information from the lower atmospheric parts, we were able to detect the vertical abundance gradient of magnesium and possibly silicon.

Our study provides additional evidence that the light variability of chemically peculiar stars is in most cases caused by

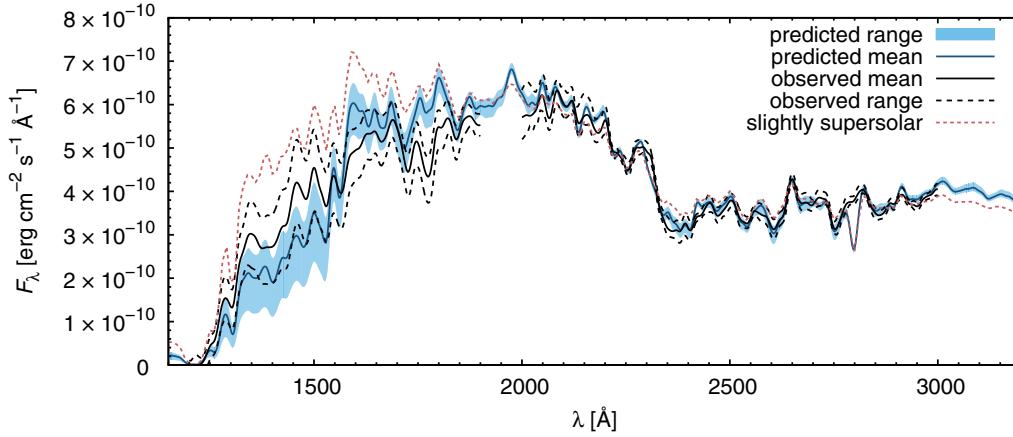


Fig. 13. Comparison of the predicted flux (mean and its variation, blue) with corresponding observed quantities (black). The predicted and observed fluxes (IUE) were smoothed by a Gaussian filter with a dispersion of 10 \AA . Overplotted is the flux calculated for a slightly supersolar chemical composition with $\epsilon_{\text{Mg}} = -4.1$, $\epsilon_{\text{Si}} = -3.7$, $\epsilon_{\text{Cr}} = -5.9$, $\epsilon_{\text{Mn}} = -5.7$, and $\epsilon_{\text{Fe}} = -4.2$.

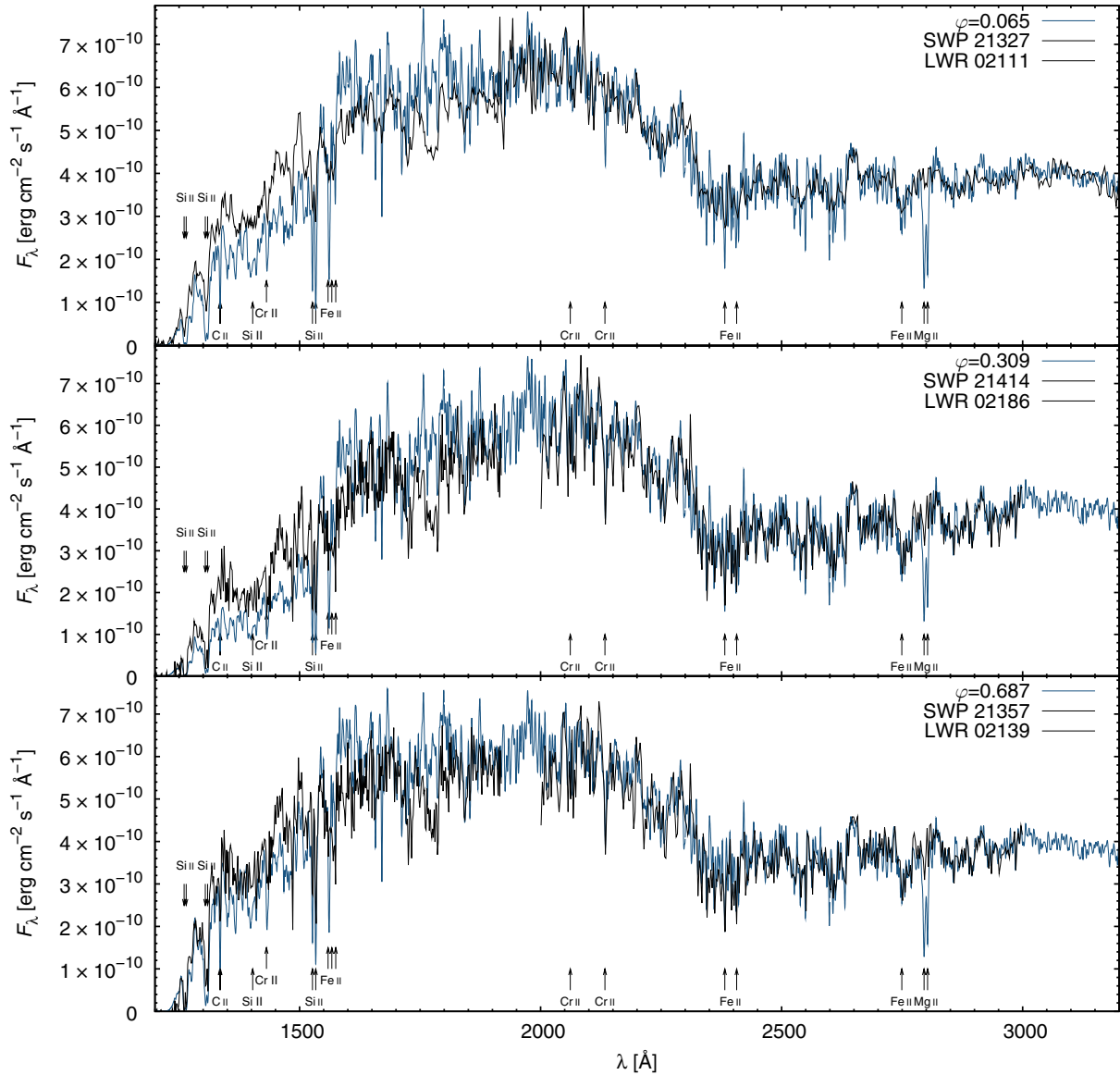


Fig. 14. Predicted and observed (IUE) flux in selected phases. Predicted fluxes were smoothed by a Gaussian filter with a dispersion of 1.3 \AA . Individual strong lines and iron line blends are identified.

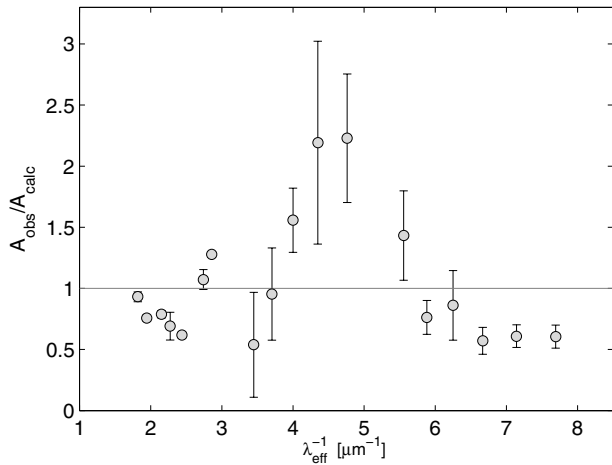


Fig. 15. Comparison of the amplitudes of the observed photometric variability and the variability predicted by the physical model. The real variability is in most cases weaker with some exception when it is strengthened by the role of the secondary spot at the phase 0.11.

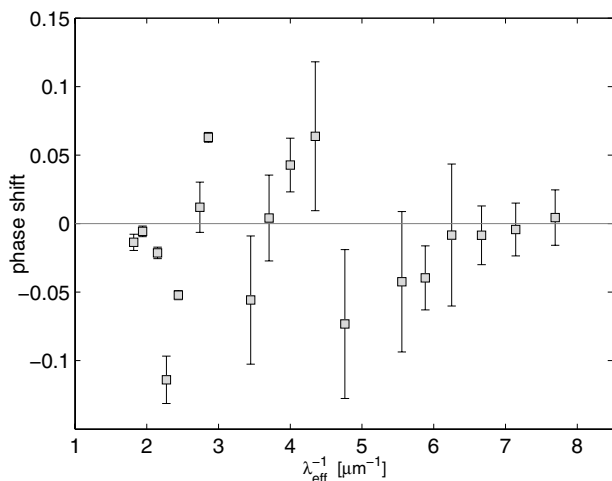


Fig. 16. Dependence of the phase shift between the observed and predicted light curves. Note the well documented jump in the shift in the region of the Balmer jump. See also the shapes of observed and predicted light curves in Fig. 10.

the inhomogeneous surface distribution of individual chemical elements and flux redistribution and is modulated by the stellar rotation. For cooler chemically peculiar stars in addition to silicon and iron, other iron-peak elements also influence the light variability, in our case, mostly chromium. The comparison of the observed and predicted spectral energy distribution was able to reveal all missing opacities in the model atmospheres.

Acknowledgements. This research was partly based on the IUE data derived from the INES database using the SPLAT package and has made use of the NIST spectral line database (Kramida et al. 2013). This work was supported by the grant GA ČR P209/12/0217 and by a mobility grant of MŠMT 7AMB14AT015 (WTZ CZ 09/2014). T. Lüftinger acknowledges the support by the FWF NFN project S116601-N16 and the related FWF NFN subproject, S116 604-N16.

References

- Adelman, S. J. 1997, *A&A*, **122**, 249
 Adelman, S. J., & Kaewkorommaung, P. 2005, *A&A*, **435**, 1099
 Asplund, M., Grevesse, N., Sauval, A. J., & Scott, P. 2009, *ARA&A*, **47**, 481
 Aurière, M., Wade, G. A., Silvester, J., et al. 2007, *A&A*, **475**, 1053
 Babu, G. S. D. 1977, *Ap&SS*, **50**, 343
 Bailey, J. D., & Landstreet, J. D. 2013, *A&A*, **551**, A30
 Balona, L. A. 2013, *MNRAS*, **431**, 2240
 Bessell, M. S. 2011, *PASP*, **123**, 1442
 Borra, E. F., & Landstreet, J. D. 1980, *ApJS*, **42**, 421
 Castelli, F. 2005, *Mem. Soc. Astron. It. Supp.*, **8**, 25
 Cowley, A., Cowley, C., Jaschek, M., et al. 1969, *AJ*, **74**, 375
 ESA 1997, The HIPPARCOS and Tycho Catalogs (Noordwijk, The Netherlands: ESA Publication Division)
 Hatzes, A. P. 1991, *MNRAS*, **248**, 487
 Khan, S. A., & Shulyak, D. 2007, *A&A*, **469**, 1083
 Khokhlova, V. L., Rice, J. B., & Wehlauf, W. H. 1986, *ApJ*, **307**, 768
 Kramida, A., Ralchenko, Yu., Reader, J., & NIST ASD Team 2013, NIST Atomic Spectra Database, version 5.1, <http://physics.nist.gov/asd>
 Krtička, J., Mikulášek, Z., Henry, G. W., et al. 2009, *A&A*, **499**, 567
 Krtička, J., Mikulášek, Z., Lüftinger, T., et al. 2012, *A&A*, **537**, A1
 Kupka, F., Paunzen, E., & Maitzen, H. M. 2003, *MNRAS*, **341**, 849
 Kurucz, R. L. 2005, *Mem. Soc. Astron. It. Supp.*, **8**, 14
 Kuschnig R. 1998a, Ph.D. Thesis, Univ. of Vienna
 Kuschnig, R. 1998b, *Contributions of the Astronomical Observatory Skalnaté Pleso*, **27**, 418
 Landstreet, J. D., & Borra, E. F. 1977, *ApJ*, **212**, L43
 Lanz, T., & Hubeny, I. 2007, *ApJS*, **169**, 83
 Lanz, T., Artru, M.-C., Le Dourneuf, M., & Hubeny, I. 1996, *A&A*, **309**, 218
 Lignières, F., Petit, P., Böhm, T., & Aurière, M. 2009, *A&A*, **500**, L41
 Lüftinger, T., Kochukhov, O., Ryabchikova, T., et al. 2008, *Contributions of the Astronomical Observatory Skalnaté Pleso*, **38**, 335
 Lueftinger, T., Kuschnig, R., Piskunov, N. E., & Weiss, W. W. 2003, *A&A*, **406**, 1033
 Michaud, G. 2004, in The A-Star Puzzle, eds. J. Zverko, J. Žižňovský, S. J. Adelman, & W. W. Weiss (Cambridge: Cambridge Univ. Press), *IAU Symp.*, **224**, 173
 Michaud, G., Richer, J., & Vick, M. 2011, *A&A*, **534**, A18
 Mihalas D. 1978, *Stellar Atmospheres* (San Francisco: Freeman & Co.)
 Mikulášek, Z. 2007, *Astron. & Astrophys. Transact.*, **26**, 63
 Mikulášek, Z., Krtička, J., Henry, G. W., et al. 2008, *A&A*, **485**, 585
 Mikulášek, Z., Krtička, J., Henry, G. W., et al. 2011a, *A&A*, **534**, L5
 Mikulášek, Z., Zejda, M., Qian, S., & Zhu, L. 2011b, *ASP Conf. Ser.*, **451**, 111
 Molnar, M. R. 1973, *ApJ*, **179**, 527
 Nesvacil, N., Shulyak, D., Ryabchikova, T. A., et al. 2013, *A&A*, **552**, A28
 Pasinetti Fracassini, L. E., Pastori, L., Covino, S., & Pozzi, A. 2001, *A&A*, **367**, 521
 Peterson, D. M. 1970, *ApJ*, **161**, 685
 Petit, P., Lignières, F., Aurière, M., et al. 2011, *A&A*, **532**, L13
 Rice, J. B., & Wehlauf, W. H. 1991, *A&A*, **246**, 195
 Rice, J. B., Holmgren, D. E., & Bohlender, D. A. 2004, *A&A*, **424**, 237
 Romanyuk, I. I. 2007, *Astrophys. Bull.*, **62**, 62
 Ryabchikova, T., Kochukhov, O., & Bagnulo, S. 2008, *A&A*, **480**, 811
 Shulyak, D., Valyavin, G., Kochukhov, O., et al. 2007, *A&A*, **464**, 1089
 Shulyak, D., Krtička, J., Mikulášek, Z., Kochukhov, O., & Lüftinger, T. 2010, *A&A*, **524**, A66
 Shulyak, D., Paladini, C., Causi, G. L., Perraut, K., & Kochukhov, O. 2014, *MNRAS*, **443**, 1629
 Silvester, J., Wade, G. A., Kochukhov, S., et al. 2012, *MNRAS*, **426**, 1003
 Trasco, J. D. 1972, *ApJ*, **171**, 569
 van Leeuwen, F. 2007, *A&A*, **474**, 653
 Vauclair, S. 2003, *Ap&SS*, **284**, 205
 Wade, G. A., Donati, J.-F., Landstreet, J. D., & Shorlin, S. L. S. 2000, *MNRAS*, **313**, 851
 Wamsteker, W., Skillen, I., Ponz, J. D., et al. 2000, *Ap&SS*, **273**, 155
 Winzer, J. E. 1974, Ph.D. Thesis, Univ. Toronto
 Wolff, S. C., & Wolff, R. J. 1971, *AJ*, **76**, 422